Large trigonal-field effect on spin-orbit coupled states in a pyrochlore iridate

Daisuke Uematsu,[1,][*] Hajime Sagayama,[1] Taka-hisa Arima,[1,2] Jun J. Ishikawa,[3] Satoru Nakatsuji,[3,4] Hidenori Takagi,[5]
Masahiro Yoshida,[6,7] Jun'ichiro Mizuki,[6,7] and Kenji Ishii[6]

[1]*Department of Advanced Materials Science, The University of Tokyo, 5-1-5 Kashiwanoha, Kashiwa, Chiba 277-8561, Japan*
[2]*RIKEN Center for Emergent Matter Science (CEMS), Wako 351-0198, Japan*
[3]*Institute for Solid State Physics, University of Tokyo, Kashiwa, Chiba 277-8581, Japan*
[4]*PRESTO, Japan Science and Technology Agency (JST), 4-1-8 Honcho Kawaguchi, Saitama 332-0012, Japan*
[5]*Department of Physics, University of Tokyo, Bunkyo, Tokyo 113-8656, Japan*
[6]*SPring-8, Japan Atomic Energy Agency, Sanda 679-5148, Japan*
[7]*School of Science and Technology, Kwansei Gakuin University, Hyogo 669-1337, Japan*

The half-filled topmost valence band of Ir^{4+} in several iridates such as Sr_2IrO_4, IrO_2, and $CaIrO_3$ has been proposed to originate mainly from the spin-orbit coupled $J_{eff} = 1/2$ states. In pyrochlore iridates $R_2Ir_2O_7$ (R: rare earth), some exotic electronic states are theoretically proposed by assuming $J_{eff} = 1/2$ states. However, the octahedral coordination around Ir is trigonally distorted, which may affect the energy level scheme of Ir $5d$ states. Here, we report spectra of resonant elastic and inelastic x-ray scattering in $Eu_2Ir_2O_7$ at the Ir L edges. A large suppression of the magnetic scattering signal at the Ir L_{II} edge supports the $J_{eff} = 1/2$ picture rather than the $S = 1/2$ one. The inelastic scattering spectrum indicates that the magnitude of the trigonal field on the Ir^{4+} states is evaluated to be comparable to the spin-orbit interaction. The energy diagram of the $5d$ state is proposed based on the simple cluster model.

I. INTRODUCTION

Recently, the effect of strong spin-orbit (SO) coupling in $5d$ transition-metal oxide compounds has been attracting the attention of condensed-matter scientists. A layered perovskite-type iridate Sr_2IrO_4 is a good example of a spin-orbital entangled Mott insulator. The complex $5d$ $J_{eff} = 1/2$ states arise from strong spin-orbit coupling [1,2] and are split from the $J_{eff} = 3/2$ states, thereby reducing the effective width of the $5d$ conduction band. As a result, electrons are localized by a moderate Coulomb repulsion. Most of the pyrochlore iridates $R_2Ir_2O_7$ (R = Y, Nd-Lu) also show an insulating behavior below a T_{MI} of 32–120 K [3,4], which is thought to originate from an interplay between spin-orbit coupling and electron correlations. In fact, the increase in the ionic radius of R^{3+} suppresses the divergence of the resistivity at low temperatures, because of the enhanced interatomic hopping of $5d$ electrons of Ir^{4+} through the bending Ir-O-Ir bond rather than by a direct overlapping [3]. An Ir L_{III}-edge resonant x-ray scattering (RXS) experiment in $Eu_2Ir_2O_7$ has revealed that the insulating phase exhibits noncollinear magnetic ordering, referred to as an all-in/all-out structure, where all the moments of Ir^{4+} on each tetrahedron in the pyrochlore lattice are pointing toward or outward from the center of the tetrahedron [5]. The magnetic structure is the same as that in a pyrochlore osmate $Cd_2Os_2O_7$, which also undergoes a metal-insulator transition [6,7]. Considering that the transition temperature surpasses the Weiss temperature in the iridates and the osmate [8], it seems that the geometrical frustration inherent in the pyrochlore lattice is relaxed without lattice distortion. A possible scenario is that the Dzyaloshinskii-Moriya interaction stabilizes the noncollinear all-in/all-out magnetic ordering.

Another possible origin is the single-ion magnetic anisotropy caused by a deviation of the Ir^{4+} states from the isotropic $J_{eff} = 1/2$ states. In fact, the cubic O_h symmetry declines into trigonal D_{3d} in each IrO_6 of $R_2Ir_2O_7$, which could lift the degeneracy of $J_{eff} = 3/2$ states and cause a slight hybridization with a higher-lying half-filled $J_{eff} = 1/2$ orbital. Nonzero anisotropic tensor of susceptibility (ATS) scattering was observed at the Ir L_{III} edge as a consequence of the trigonal distortion of IrO_6 octahedra [5].

An $R_2Ir_2O_7$ system has been also investigated in terms of exotic topological electronic states [9–14]. Pesin and Balents pointed out that pyrochlore iridates should be good candidates for a topological Mott insulator, which should exhibit gapless spin excitations at the surfaces. Yang and Kim investigated the electronic structure and found that the trigonal crystal field is an essential parameter for the metal-to-topological insulator transition. Kargarian and co-workers showed a rich phase diagram, where several exotic topological phases compete with each other. Wan and co-workers performed a local density approximation (LDA)+U calculation and argued that a topological semimetallic state (Weyl semimetal) could be realized. These theoretical studies indicate that the experimental estimation of the local trigonal field in pyrochlore iridate compounds is necessary to discuss the electronic states. Recently, Hozoi and co-workers reported a resonant inelastic x-ray scattering (RIXS) spectrum of pyrochlore iridates and found that the trigonal field is as large as 0.4–0.6 eV [15]. However, their samples were metallic down to the lowest temperature and hence the off-stoichiometry effect could not be excluded. In other words, the effect of the trigonal field in the insulating pyrochlore iridates is yet to be experimentally investigated. Later, the temperature dependence of RIXS across T_{MI} on a fine-quality sample, clearly showing insulating behavior, is revealed. Ir L-edge RXS and RIXS are useful probes of $5d$ electronic states, because dipole transitions are

───────
[*]uematsu@cor.k.u-tokyo.ac.jp

allowed between $2p$ core states and $5d$ states. Here, we report the branching ratio of RXS and spectra of RIXS in $Eu_2Ir_2O_7$, where magnetic moments are hosted only by Ir ions. The magnetic scattering becomes quite inferior to the ATS scattering in intensity at the L_{II} edge, and the spin state of the outermost electrons of Ir^{4+} is confirmed to be strongly coupled with the orbital angular momentum $\boldsymbol{l}$. The L_{III}-edge RIXS spectrum shows that the ideally fourfold $J_{eff} = 3/2$ states are split in energy, in contrast to the previous RIXS data on Sr_2IrO_4 [16,17]. This result suggests a reconstruction of the higher-lying $J_{eff} = 1/2$ and the lower-lying $J_{eff} = 3/2$ bands. An IrO_6-cluster crystal-field calculation, in which O^{2-} anions are treated as point charges, succeeds in reproducing the peak positions in the obtained RIXS spectra within experimental uncertainty. The energy scale of the trigonal ligand field is of the same magnitude as the atomic spin-orbit interaction of iridium.

II. EXPERIMENTAL

Single crystals of $Eu_2Ir_2O_7$ were grown by a KF flux method. Detailed information is given elsewhere [4,18]. Powder and single-crystal x-ray diffraction analyses confirmed that the crystals have a pyrochlore structure with a lattice constant $a = 10.274(3)$ Å. A measurement of RXS was carried out by using a seven-circle diffractometer installed on BL-3A, Photon Factory, High Energy Accelerator Research Organization, Japan. A high-quality crystal with a flat triangular (111) surface with edges about 0.5 mm long with an inverse resistivity ratio of $\rho(2\,K)/\rho(300\,K) = 7600$ was selected for the present RXS measurement. The composition ratio y of Eu to Ir is expected to deviate by less than 5% from the stoichiometry [4]. The crystal was attached to a copper plate with varnish and mounted in a closed-cycle ^{4}He refrigerator. An x-ray beam with the horizontal polarization from an undulator source was monochromatized by a Si(111) double crystal. The sample was oriented such that the [011] axis is parallel to the polarization vector of the beam and perpendicular to the scattering plane (so-called σ polarization). In this configuration, RXS caused by the all-in/all-out magnetic order should be polarized in the scattering plane (π' polarization), while that caused by the local anisotropies at the Ir sites is perpendicular to the plane (σ' polarization). To separate these contributions, we analyzed the polarization of the scattered x ray by using a Mo or pyrolytic graphite (PG) analyzer for Ir L_{III} and L_{II} edges, respectively. The 2θ value of Mo(400) reflection at 11.23 keV is $89°$, and that of PG(10 0 0) reflection at 12.85 keV is $92°$, which guarantees a polarization purity of higher than 99.8%. A RIXS measurement was performed on BL11XU at SPring-8, Japan. A crystal with a Eu/Ir ratio y of 0.98(2), which was estimated by electron probe microanalyses (EPMA), was selected for the RIXS measurement. A previous study on the effect of nonstoichiometry on the physical properties in $Eu_2Ir_2O_7$ [4] clearly showed that crystals with an off-stoichiometry of less than 5% should exhibit a sharp metal-insulator transition. Incident x rays were monochromatized to be 11.22 keV, which corresponds to the Ir L_{III} edge, by a double-crystal Si(111) monochromator, and a secondary Si(844) channel-cut crystal was used to reduce the energy width. The polarization of the incident beam was set parallel to the scattering plane. Scattered
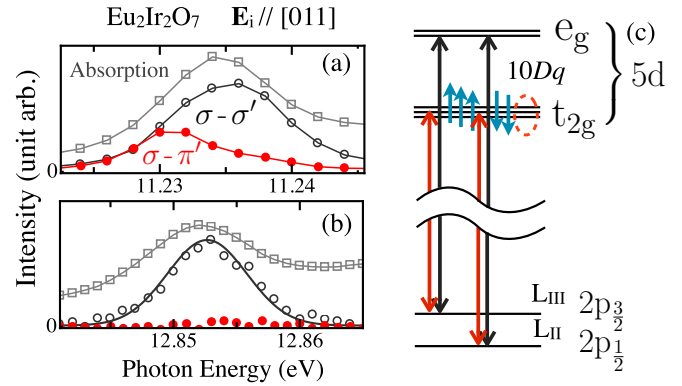

FIG. 1. (Color online) Spectra of x-ray absorption (open squares) and (10 0 0) scattering intensities at (a) L_{III} and (b) L_{II} edges at 50 K. The scattering was decomposed into σ-σ' (open circles) and σ-π' (solid circles) channels, which can be ascribed to the anisotropic orbitals and magnetic moments in Ir $5d$ states, respectively (see text). Solid lines are guides to eye. The diffraction intensity data shown here are corrected by absorption. (c) Schematic diagram for the resonant processes between $5d$ valence and $2p$ core states.

x rays were analyzed in energy by a spherically bent Si(844) crystal. The total energy resolution estimated from the full width at half maximum of the elastic peak was about 70 meV. RIXS at momentum transfers around (10 6 6) were detected, so that the scattering angle 2θ is close to $90°$ in order to reduce the elastic scattering. The incident and scattered polarizations are therefore roughly orthogonal to each other, which is the so-called depolarized configuration.

III. RESULTS AND DISCUSSIONS

Figures 1(a) and 1(b) show spectra of RXS at 50 K as well as x-ray absorption spectra at the L_{III} and L_{II} edges of iridium. Here, the effect of absorption on the apparent x-ray scattering intensity was corrected. In general, the octahedral field $10Dq$ in iridates is much larger than the Hund's coupling, resulting in a low-spin configuration. Because each Ir^{4+} ion has five $5d$ electrons, a major resonant enhancement of the magnetic scattering (σ-π' channel) is expected to appear only at the $2p$-t_{2g} transitions. On the other hand, the orbital shapes of both the e_g and t_{2g} states can be modulated by the trigonal distortion of each IrO_6 octahedron, indicating that the ATS scattering should be enhanced also by the resonance with the $2p$-e_g transitions. The difference in the resonant process between the magnetic and ATS scattering shows up as the deviation of the peak position in Fig. 1(a). We can evaluate the octahedral ligand field ($10Dq$) to be 3–5 eV from the difference in the peak position between the two channels. The L_{II}-edge RXS data show that the intensity ratio of magnetic to ATS at (10 0 0) is smaller than 6%, as shown in Fig. 1(b). This result implies that the unpaired $5d$ electron at each Ir^{4+} site can be represented by the so-called $J_{eff} = 1/2$ states in the first approximation rather than the orbital momentum quenched $S = 1/2$ states. The presence of a $J_{eff} = 1/2$ ground state supports our RIXS results mentioned later as well.

Figure 2 shows spectra of RIXS of $Eu_2Ir_2O_7$. The Ir L_{III}-edge RIXS is sensitive to $5d$-$5d$ excitations because
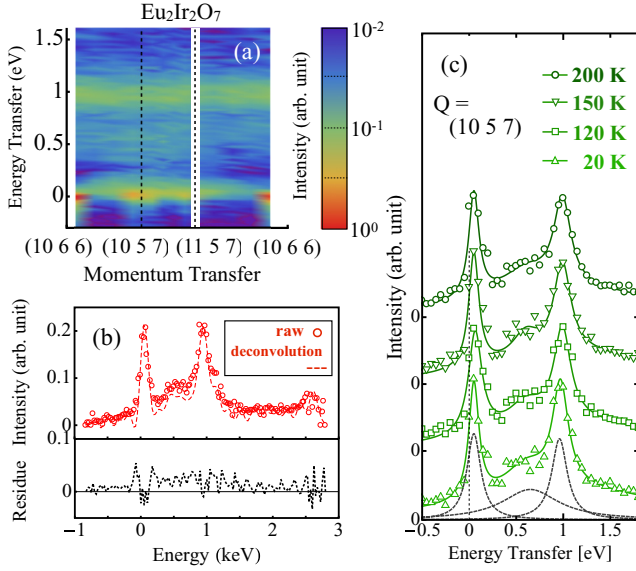
FIG. 2. (Color online) (a) Contour map of resonant inelastic x-ray scattering (RIXS) intensity of $Eu_2Ir_2O_7$ at 20 K with sweeping the momentum transfer along high-symmetry lines. There is no distinctive dispersion within the energy resolution and it appears as fairly flat bands. (b) Peak profile with dotted line for deconvolution at $Q = (10\ 6.25\ 5.75)$, below which numerical residue is depicted. (c) Temperature dependence of the RIXS intensity as a function of energy transfer at a fixed wave vector of $(0\bar{1}1)$ in the Brillouin zone. Two clear peaks are observed in the vicinity of 0 and 1 eV, and in between them a vague broad peak is discerned.

of large transition probabilities between $2p$ and $5d$. Each spectrum below 1.8 eV is characterized by two sharp peaks at energy transfers $\Delta E \approx 0$ and 1.0 eV and a broad hump between them, as shown by the dotted lines in Fig. 2(b). It is of note here that such a hump is not observed in Sr_2IrO_4 [17]. As shown in Fig. 2(a), the dispersion of each band is smaller than 0.1 eV. Localized $5d$ orbitals hence may be a good starting point to understanding the spectrum. RIXS measurements are performed on a high-quality crystal, which clearly exhibits insulating behavior at low temperatures and shows no temperature dependence across T_{MI} [Fig. 3(c)]. Assuming the peak just above 0 eV would be smeared out with elastic scattering, we will not discuss this further. The peaks at 0.5 and 1 eV cannot be explained by the t_{2g}-e_g excitation, because the ligand field is estimated to be much larger, as mentioned above. The most possible origin would be excitations between the $J_{eff} = 1/2$ and $J_{eff} = 3/2$ states among the t_{2g} manifold [17]. We analyzed the spectrum by a simple IrO_6 cluster model, considering the crystal field (CF) $\mathcal{H}_{CF}$ and atomic spin-orbit coupling $\mathcal{H}_{SO} = \xi\, \boldsymbol{l}\cdot\boldsymbol{s}$. Using the polar coordinate, where the local trigonal axis orients along z [see Fig. 3(a)], $\mathcal{H}_{CF}$ is expanded in terms of spherical harmonics Y_n^m as

$$\mathcal{H}_{CF} = 6Ze^2 \left(\frac{r^2}{R^3} \frac{4}{5}\pi\; Y_2^0(\theta,\phi) A_{20} \right.$$

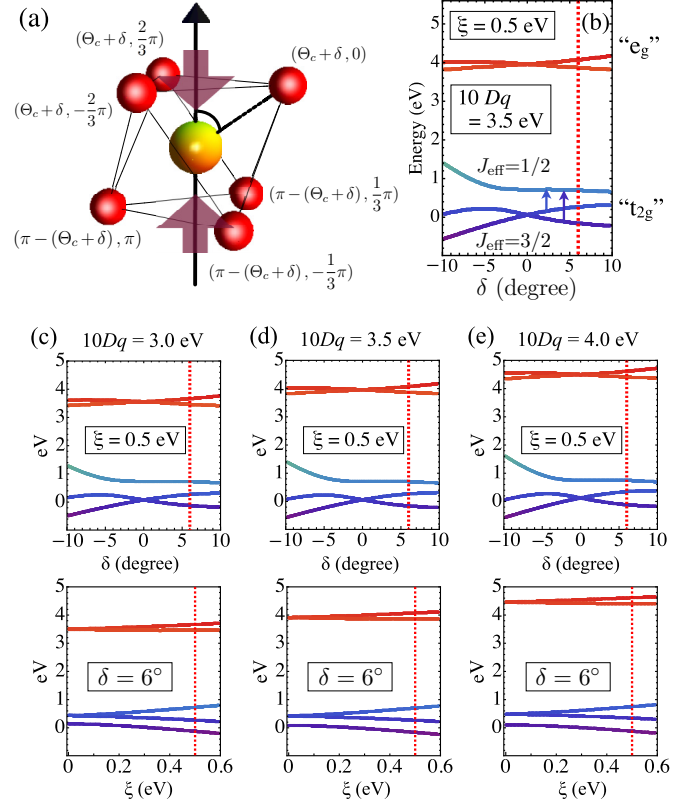$$\left. + \frac{r^4}{R^5}\frac{4}{9}\pi \sum_{m=0,\pm3} Y_4^m(\theta,\phi) A_{4m} \right). \tag{1}$$

FIG. 3. (Color online) (a) Positions of six O^{2-} ligands of trigonally distorted IrO_6 in the polar coordinates. δ represents the distortion of IrO_6 in degrees. (b) Energy scheme of Ir $5d$ with respect to δ in IrO_6. The vertical dotted line indicates the δ value obtained by a synchrotron x-ray crystal-structure analysis. (c)–(e) Energy scheme with respect to δ for $\xi = 0.5$ eV (upper) and with respect to SO coupling ξ for $\delta = 6°$ (lower) for $10Dq = 3.0$, 3.5, and 4.0 eV, respectively.

Here, each oxygen atom is regarded as a point charge of $-Ze$ and $R = 2.03$ Å is the Ir-O bond length. $A_{nm} \equiv Y_n^m(\Theta_c + \delta, 0)$, where $\Theta_c + \delta$ represents the Ir-O bond direction measured from the trigonal axis. According to our structural analysis on a single crystal of $Eu_2Ir_2O_7$ [5], the Ir-O bond direction is modified from the case of the regular octahedron Θ_c by $\delta = +5.9°$. In this expansion, the octahedral field is $10Dq$, which is energy splitting at $\delta = 0$. The total Hamiltonian can be expressed as $\frac{5Ze^2\langle r^4\rangle}{3R^5}(\leftrightarrow A_{43}/A_{40} = \sqrt{10/7})$, where

$$\mathcal{H} = \mathcal{H}_{LS} + \mathcal{H}_{CF} = \xi \mathbf{Q}_{LS} + Ze^2 \frac{\langle r^4\rangle}{R^5}\frac{8}{3}\pi (A_{40}\mathbf{Q}_{40} + A_{43}\mathbf{Q}_{43})$$

$$+ Ze^2 \frac{\langle r^2\rangle}{R^3}\frac{24}{5}\pi A_{20}\mathbf{Q}_{20}, \tag{2}$$

$$\mathbf{Q}_{43} = \frac{-1}{14\sqrt{\pi}} \begin{pmatrix} & & & -\sqrt{35} & 0 \\ & & & & \sqrt{35} \\ & & 0 & & \\ -\sqrt{35} & & & & \\ 0 & \sqrt{35} & & & \end{pmatrix},$$

$$\mathbf{Q}_{40} = \frac{-1}{14\sqrt{\pi}} \begin{pmatrix} -1 & & & \\ & 4 & & 0 \\ & & -6 & \\ & 0 & & 4 \\ & & & & -1 \end{pmatrix},$$

$$\mathbf{Q}_{20} = \frac{-1}{14\sqrt{\pi}} \begin{pmatrix} 2\sqrt{5} & & & \\ & -\sqrt{5} & & 0 \\ & & -2\sqrt{5} & \\ & 0 & & -\sqrt{5} \\ & & & & 2\sqrt{5} \end{pmatrix}.$$

Estimation for the eigensystems of the $5d$ electron accounts for spin-orbit coupling ξ, octahedral crystal field $10Dq$, and trigonal distortion in IrO$_6$. The parameters that we used for the calculation were $\xi = 0.5$ eV [19] and $10Dq = 3.5$ eV. We also set $Z\langle r^2 \rangle \approx Z\langle r^4 \rangle / R^2$ (≈ 1.22 Å^2). We plot the eigenenergies of Eq. (2) against δ in Fig. 3(b). Here, each line represents a Kramers doublet, because the exchange interaction is not considered. In the case of the regular-octahedral coordination ($\delta = 0$), the t_{2g} states are split into a doublet and a quartet, corresponding to the $J_{\mathrm{eff}} = 1/2$ and $3/2$ states, respectively. With increasing δ (compressive trigonal distortion), the $J_{\mathrm{eff}} = 3/2$ states as well as the e_g states at an energy higher by about $10Dq$ start to be split into two doublets. The triple-peak structure in the RIXS spectra shown in Fig. 2 is explained based on the electronic diagram. The split of the J_{eff} states may cause two kinds of excitations to the half-filled $J_{\mathrm{eff}} = 1/2$ states, as indicated by the arrows in Fig. 3(b). Furthermore, low-energy excitations may emerge among the partially filled $J_{\mathrm{eff}} = 1/2$ states. Because the peak positions in the experimental spectrum shown in Fig. 2 are well reproduced by the calculated energy levels at $\delta = 5.9°$ in Fig. 3(b), the values of the parameters are fairly well accepted. Although there are several uncertainties in the values of the parameters, the above-mentioned overall feature is not affected by the parameters. The effects of the octahedral field $10Dq$ and spin-orbit coupling ξ on the electronic level scheme are shown in Figs. 3(c)–3(e). The sixfold degeneracy in the t_{2g} levels is lifted by the spin-orbit interaction ξ and the trigonal field, which is insensitive to the value of $10Dq$. The spin-orbit interaction would split t_{2g} into a higher-lying doublet and a lower-lying quartet, while the compressive trigonal distortion ($\delta > 0$) would split t_{2g} into a higher-lying quartet and a lower-lying doublet (see the levels at $\xi = 0$). The energy separation in the t_{2g} state at $\xi = 0$ is interpreted as the trigonal field in distorted IrO$_6$. The peak profile in RIXS data and the eigenvalues for the virtual state, in accordance with the crystal-structure analysis indicated by the red dotted lines in Fig. 3(d), numerically derived from the given Hamiltonian, are in good agreement with each other.

The trigonal crystal field Δ_{tri} is estimated to be ~ 0.45 eV when $10Dq = 3.5$ eV. The Δ_{tri} value become larger as $10Dq$ increases, as shown in Figs. 3(c)–3(e). It is noteworthy that Δ_{tri} is as large as the typical atomic spin-orbit interaction of iridium, ~ 0.5 eV. The wave function of the $J_{\mathrm{eff}} = 1/2$ level is represented as

$$\psi_{\pm 3} = \pm a_0 \left| Y_2^0, \mp \sigma \right\rangle \pm a_1 \left| Y_2^{\mp 1}, \pm \sigma \right\rangle - a_2 \left| Y_2^{\pm 2}, \pm \sigma \right\rangle. \quad (3)$$

Here, we use a local Cartesian coordinate system $\hat{x}, \hat{y}, \hat{z}$. The $\hat{z}$ axis is set parallel to the principal axis of trigonal distortion
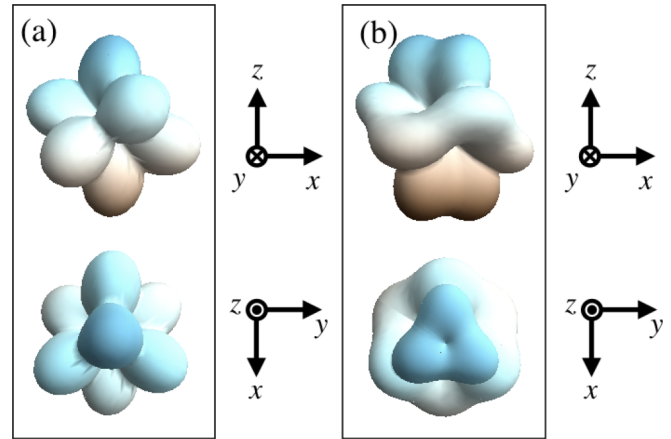

FIG. 4. (Color online) (a) Illustration for $J_{\mathrm{eff}} = 1/2$ and (b) calculated wave function of the $5d$ hole near the Fermi level of Eu$_2$Ir$_2$O$_7$ projected along the local y (top) and z (bottom) axes.

[the black arrow in Fig. 3(a)], which is also parallel to the ordered magnetic moment. When $\delta = 0$, $a_0 = 1/\sqrt{3}$, $a_1 = \sqrt{2}/3$, and $a_2 = 2/3$. We found that the trigonal compressive strain should increase a_1 and reduce a_2. When $\delta = 5.9°$, $a_0 = 0.58$, $a_1 = 0.59$, and $a_2 = 0.56$. The modification of the eigenstate is schematically shown in Fig. 4. The variations in a_1 and a_2 significantly suppress $|\langle l_z \rangle|$, while they do not affect $|\langle s_z \rangle|$ very much. As a result, the fluctuation of the orbital angular momentum $\boldsymbol{l}$ in the xy plane grows, and the $5d$ hole tends to transfer to the O $2p$ states with the orbital angular momentum $\boldsymbol{l}$ parallel to the bond direction. This orbital selective transfer may stabilize the all-in/all-out magnetic order in the pyrochlore lattice, which is generally believed to host geometrical frustration.

The trigonal field also modifies the two higher-lying doublets relevant to the e_g states. The anisotropic wave functions are the major source of ATS scattering at the Ir $L_{\mathrm{II,III}}$ edges, as shown in Fig. 1. A continuous change in the intensity of ATS scattering across the phase transition has been reported in Ref. [5], which also supports a small change in the electron level scheme at the phase transition. We further investigated the temperature dependence of the electronic structure. While Eu$_2$Ir$_2$O$_7$ undergoes a transition between a paramagnetic metal phase and an all-in/all-out insulating phase at $T_{\mathrm{MI}} \simeq 120$ K [3,4], the RIXS spectrum is almost independent of temperature, as shown in Fig. 2(b). This result implies that the metal-insulator transition should arise from a reconstruction of the electronic states within the $J_{\mathrm{eff}} = 1/2$-derived doublet. The present RIXS data show no clear change, even in the lowest-lying peak across the transition. A further study with a much higher-energy resolution is needed to detect the possible change.

Finally, we evaluate the intensities of the magnetic and ATS scattering at L_{II} and L_{III}. The higher-lying e_g states vary to

$$\psi_{5\pm} = 0.78 \left| Y_2^{\pm 2}, \pm \sigma \right\rangle \mp 0.62 \left| Y_2^{\mp 1}, \pm \sigma \right\rangle \mp 0.11 \left| Y_2^0, \mp \sigma \right\rangle \quad (4)$$

TABLE I. Polarization vectors of incident (scattered) x rays for the local coordination of each Ir^{4+} sublattice.

	$\hat{\epsilon}_{in} \parallel [100]$	$\hat{\epsilon}_{out} \parallel [01\bar{1}]$
$[111]$	$\frac{1}{\sqrt{2}}, \frac{1}{\sqrt{6}}, \frac{1}{\sqrt{3}}$	$-\frac{1}{2}, \frac{\sqrt{3}}{2}, 0$
$[1\bar{1}\bar{1}]$	$-\frac{1}{\sqrt{2}}, -\frac{1}{\sqrt{6}}, \frac{1}{\sqrt{3}}$	$-\frac{1}{2}, \frac{\sqrt{3}}{2}, 0$
$[\bar{1}1\bar{1}]$	$\frac{1}{\sqrt{2}}, \frac{1}{\sqrt{6}}, -\frac{1}{\sqrt{3}}$	$\frac{1}{2}, \frac{1}{\sqrt{12}}, \frac{2}{\sqrt{6}}$
$[\bar{1}\bar{1}1]$	$-\frac{1}{\sqrt{2}}, -\frac{1}{\sqrt{6}}, -\frac{1}{\sqrt{3}}$	$\frac{1}{2}, \frac{1}{\sqrt{12}}, -\frac{2}{\sqrt{6}}$

and

$$\psi_{4\pm} = 0.20 \left| Y_2^{\mp 2}, \pm\sigma \right\rangle \mp 0.59 \left| Y_2^{\pm 2}, \mp\sigma \right\rangle + 0.78 \left| Y_2^{\mp 1}, \mp\sigma \right\rangle, \tag{5}$$

with a trigonal distortion of $\delta = 5.9°$. These states contribute to the anomalous scattering of the x ray near the $L_{II,III}$

edges of Ir. The anisotropic anomalous scattering factors for an Ir^{4+} ion at the L_{III} and L_{II} edges are calculated as

$$f_{\alpha\alpha}^{(n)}(L_{III}) \sim \sum_{m=-\frac{3}{2}}^{\frac{3}{2}} \frac{\left| \left\langle 2p_{3/2}^m \left| \alpha \right| R_{5d}(r)\psi_n \right\rangle \right|^2}{\hbar\omega - \left(E_n - E_{2p_{3/2}} \right)} \tag{6}$$

and

$$f_{\alpha\alpha}^{(n)}(L_{II}) \sim \sum_{m=-\frac{1}{2}}^{\frac{1}{2}} \frac{\left| \left\langle 2p_{1/2}^m \left| \alpha \right| R_{5d}(r)\psi_n \right\rangle \right|^2}{\hbar\omega - \left(E_n - E_{2p_{1/2}} \right)}, \tag{7}$$

respectively, where $n = 5+, 5-, 4+$, or $4-$. The polarization of the x ray is represented by α (unit vector $\hat{x}$, $\hat{y}$, or $\hat{z}$). The magnetic scattering factors for an Ir^{4+} ion with a magnetic moment pointing in the local $\hat{z}$ direction are similarly calculated as

$$f_{\hat{\epsilon}_{in}\hat{\epsilon}_{out}}^{mag}(L_{III}) \sim \sum_{m=-\frac{3}{2}}^{\frac{3}{2}} \frac{\left| \left\langle R_{5d}(r)\psi_3 \left| \hat{\epsilon}_{out} \cdot \hat{r} \right| 2p_{3/2}^m \right\rangle \left\langle 2p_{3/2}^m \left| \hat{\epsilon}_{in} \cdot \hat{r} \right| R_{5d}(r)\psi_3 \right\rangle \right|}{\hbar\omega - \left(E_3 - E_{2p_{3/2}} \right)} \tag{8}$$

and

$$f_{\hat{\epsilon}_{in}\hat{\epsilon}_{out}}^{mag}(L_{II}) \sim \sum_{m=-\frac{1}{2}}^{\frac{1}{2}} \frac{\left| \left\langle R_{5d}(r)\psi_3 \left| \hat{\epsilon}_{out} \cdot \hat{r} \right| 2p_{1/2}^m \right\rangle \left\langle 2p_{1/2}^m \left| \hat{\epsilon}_{in} \cdot \hat{r} \right| R_{5d}(r)\psi_3 \right\rangle \right|}{\hbar\omega - \left(E_3 - E_{2p_{1/2}} \right)}. \tag{9}$$

The structure factors for ATS and magnetic scattering at $(10\,0\,0)$ are directly calculated from these scattering factors by converting the local coordinate system (x,y,z) at each of the four Ir sites in a primitive unit cell into the global Cartesian coordinate system (a,b,c) (see Table I). The intensity ratio of the magnetic scattering in the σ-π' channel to the ATS scattering in the σ-σ' ($\hat{\epsilon}_{in} \parallel \hat{\epsilon}_{out} \parallel [01\bar{1}]$) for $(10\,0\,0)$ reflection is estimated to be 0.40 and 3.4×10^{-3} at the L_{III} and L_{II} edges, respectively. Thus the strong suppression of the magnetic scattering at the L_{II} edge is consistent with the proposed energy diagram. We also calculated the probabilities of transitions for Ir L_{III} RIXS, and found that the third peak ($\Delta E \sim 1$ eV) is larger in intensity than the second peak ($\Delta E \sim 0.5$ eV). The present results of RXS and RIXS in $Eu_2Ir_2O_7$ are hence explained by considering the trigonal field to be as large as the spin-orbit interaction.

[1] B. J. Kim, H. Jin, S. J. Moon, J.-Y. Kim, B.-G. Park, C. S. Leem, J. Yu, T. W. Noh, C. Kim, S.-J. Oh, J.-H. Park, V. Durairaj, G. Cao, and E. Rotenberg, Phys. Rev. Lett. **101**, 076402 (2008).

[2] B. J. Kim, H. Ohsumi, T. Komesu, S. Sakai, T. Morita, H. Takagi, and T. H. Arima, Science **323**, 1329 (2009).

[3] K. Matsuhira, M. Wakeshima, R. Nakanishi, T. Yamada, A. Nakamura, W. Kawano, S. Takagi, and Y. Hinatsu, J. Phys. Soc. Jpn. **76**, 043706 (2007).

[4] J. J. Ishikawa, E. C. T. O'Farrell, and S. Nakatsuji, Phys. Rev. B **85**, 245109 (2012).

[5] H. Sagayama, D. Uematsu, T. H. Arima, K. Sugimoto, J. J. Ishikawa, E. O'Farrell, and S. Nakatsuji, Phys. Rev. B **87**, 100403(R) (2013).

[6] J. Yamaura, K. Ohgushi, H. Ohsumi, T. Hasegawa, I. Yamauchi, K. Sugimoto, S. Takeshita, A. Tokuda, M. Takata, M. Udagawa, M. Takigawa, H. Harima, T. Arima, and Z. Hiroi, Phys. Rev. Lett. **108**, 247205 (2012).

[7] K. Tomiyasu, K. Matsuhira, K. Iwasa, M. Watahiki, S. Takagi, M. Wakeshima, Y. Hinatsu, M. Yokoyama, K. Ohoyama, and K. Yamada, J. Phys. Soc. Jpn. **81**, 034709 (2012).

[8] D. Yanagishima and Y. Maeno, J. Phys. Soc. Jpn. **70**, 2880 (2001).

[9] D. Pesin and L. Balents, Nat. Phys. **6**, 376 (2010).

[10] B. J. Yang and Y. B. Kim, Phys. Rev. B **82**, 085111 (2010).

[11] M. Kurita, Y. Yamaji, and M. Imada, J. Phys. Soc. Jpn. **80**, 044708 (2011).

[12] M. Kargarian, J. Wen, and G. A. Fiete, Phys. Rev. B **83**, 165112 (2011).

[13] X. Wan, A. M. Turner, A. Vishwanath, and S. Y. Savrasov, Phys. Rev. B **83**, 205101 (2011).

[14] W. Witczak-Krempa and Y. B. Kim, Phys. Rev. B **85**, 045124 (2012).

[15] L. Hozoi, H. Gretarsson, J. P. Clancy, B.-G. Jeon, B. Lee, K. H. Kim, V. Yushankhai, P. Fulde, D. Casa, T. Gog, J. Kim, A. H. Said, M. H. Upton, Y.-J. Kim, and J. van den Brink, Phys. Rev. B **89**, 115111 (2014).

[16] K. Ishii, I. Jarrige, M. Yoshida, K. Ikeuchi, J. Mizuki, K. Ohashi, T. Takayama, J. Matsuno, and H. Takagi, Phys. Rev. B **83**, 115121 (2011).

[17] J. Kim, D. Casa, M. H. Upton, T. Gog, Y.-J. Kim, J. F. Mitchell, M. van Veenendaal, M. Daghofer, J. van den Brink, G. Khaliullin, and B. J. Kim, Phys. Rev. Lett. **108**, 177003 (2012).

[18] J. N. Millican, R. T. Macaluso, S. Nakatsuji, Y. Machida, Y. Maeno, and J. Y. Chan, Mater. Res. Bull. **42**, 928 (2007).

[19] F. Ye, S. Chi, B. C. Chakoumakos, J. A. Fernandez-Baca, T. Qi, and G. Cao, Phys. Rev. B **87**, 140406(R) (2013).